

Article

Can Imaging Spectroscopy Divulge the Process Mechanism of Mineralization? Inferences from the Talc Mineralization, Jahazpur, India

Hrishikesh Kumar ^{1,*}, Desikan Ramakrishnan ², Ronak Jain ³  and Himanshu Govil ⁴

¹ Geosciences Division, Space Applications Centre, Indian Space Research Organization, Ahmedabad 380015, India

² Department of Earth Sciences, Indian Institute of Technology, Mumbai 400076, India; ramakrish@iitb.ac.in

³ School of Earth Sciences, Banasthali Vidyapith, Tonk 304022, India; jainronak75@yahoo.in

⁴ Department of Applied Geology, National Institute of Technology, Raipur 492010, India; hgovil.geo@nitrr.ac.in

* Correspondence: hrishikesh@sac.isro.gov.in

Abstract: Talc deposits of Jahazpur, Rajasthan, hosted by dolomite, are one of the largest high-quality talc deposits in India. In the present study, we use AVIRIS-NG datasets to study the link between the spatial pattern of talc mineralization, associated alteration minerals, and iron-oxide enrichment. It is noted that the majority of talc-bearing areas are characterized by the presence of clay minerals, such as an intimate mixture of kaolinite and muscovite, illite, dickite (indicative of phyllitic and argillitic alteration), and also enhanced iron enrichment. The talc-bearing zones are located adjacent to quartz-rich lithologies, and they are aligned along the Jahazpur thrust. Based on mineralogical and geological evidence, hydrothermal alteration of dolomites by silica and iron-rich fluid is proposed as major factor controlling talc mineralization. This study has implications for the identification of prospective zones of talc mineralization using imaging spectroscopy.



Citation: Kumar, H.; Ramakrishnan, D.; Jain, R.; Govil, H. Can Imaging Spectroscopy Divulge the Process Mechanism of Mineralization? Inferences from the Talc Mineralization, Jahazpur, India. *Remote Sens.* **2023**, *15*, 2394. <https://doi.org/10.3390/rs15092394>

Academic Editor: Lenio Soares Galvao

Received: 10 March 2023

Revised: 26 April 2023

Accepted: 27 April 2023

Published: 3 May 2023



Copyright: © 2023 by the authors. Licensee MDPI, Basel, Switzerland. This article is an open access article distributed under the terms and conditions of the Creative Commons Attribution (CC BY) license (<https://creativecommons.org/licenses/by/4.0/>).

Keywords: imaging spectroscopy; talc; hydrothermal alteration; mineralization

1. Introduction

Talc (hydrated magnesium silicate) is a clay mineral generally associated with metamorphic rocks along convergent plate boundaries. It may also form due to hydrothermal alteration of ultramafic rocks or dolomites or as a result of low-grade greenschist facies metamorphism of volcanogenic massive sulphides [1]. The economically viable deposits of talc are often associated with hydrothermal alteration. It is widely used in the plastic, ceramic, paper, paint, and cosmetic industry, and has significant economic importance.

ASTER has been the workhorse of the geological community for mapping alteration zones [2,3]. It could detect the geological units and broad mineral groups based on their spectral characteristics [4–10] and has played an important role in mineral exploration [11–16]. However, it is difficult to detect talc using the multispectral dataset of ASTER because of the presence of a characteristic absorption feature at 2.31 μm, which overlaps with spectrally similar calcite and dolomite [6]. ASTER has a single band centered at 2.33 μm, with a 35 nm bandwidth, therefore preventing the observation of the diagnostic doublet of talc. Hyperspectral remote sensing, also known as imaging spectroscopy, acquires reflectance of materials caused by electronic transitions and vibrational processes in narrow spectral channels of Visible to Near InfraRed (VNIR, 0.3–1.0 μm) and Short Wave InfraRed (SWIR, 1.0–2.5 μm) region spectral range 0.35–2.5 μm, and it facilitates subtle mineralogical identification and mapping [17–22]. The wavelength region, 0.3–2.5 μm, is the general spectral range of imaging spectroscopy in earth observation as iron oxides such as hematite, goethite, limonite have absorption in the VNIR region, and carbonates, mica and sulphates have their diagnostic absorption features in the SWIR region [17,19,20,23,24].

Imaging spectroscopy has shown immense potential for mineral exploration [15,25–31], characterization of acid mine drainage [32], gold exploration [33], mapping of fibrous and carcinogenic minerals [22], kimberlite detection [34], exploration of lithium bearing pegmatites [35], and the detection of alteration mineral assemblages developed due to the interaction of seeped oil/gas with the surficial cover [36]. More recently, it has led to the detection of methane plumes associated with natural and anthropogenic sources [37,38]. It is important to note that most of the abovementioned studies were carried out using airborne surveys due to a lack of high quality imaging spectroscopic datasets from satellites. However, recent launches of PRISMA and EnMAP will provide datasets over entire world and may open opportunities for a plethora of geological applications [29,39–42]. The continuity of the datasets are also guaranteed through upcoming CHIIME and HySIPRI missions [43,44].

The Jahazpur, Rajasthan hosts one of the world-class carbonate-hosted talc deposits [19,45–50]. Earlier studies carried out in the area focused on identifying pure and mixed talc [51] and identifying alteration mineral assemblages based on selected reflectance spectra [52]. However, the spatial distribution of the alteration pattern and the geological control of talc mineralization in the Jahazpur region was not studied. The present research aims to investigate hydrothermal alteration and structural and lithological control of talc mineralization in the Jahazpur region. The AVIRIS-NG hyperspectral dataset is used in the mapping of the spatial distribution of talc, dolomite (host rock), and associated alteration mineral assemblage. The Integrated Band Depth (IBD) technique [53,54] is utilized to study iron-rich zones and their association with talc mineralization. Integrated mineralogical, geological, and structural analysis and interpretation are carried out to decipher their control on talc mineralization. The identified indicators of talc mineralization in Jahazpur may help in locating prospective zones for future talc exploration in the area.

2. Study Area

The study area is situated in the Jahazpur town of Bhilwara in the district of Rajasthan, India. The area encompasses surface exposure of the Jahazpur group of rocks, which is largely composed of low-grade metasediments of the greenschist facies. These rocks are separated from the high-grade terrain of Mangalwar Complex by crustal-scale transpressive shear zone/Jahazpur thrust [55] on the western side. The Great Boundary Fault (GBF) separates the Jahazpur group of rocks from the Vindhyan sediments on the eastern side [45,47,48,56–60]. The Jahazpur belt is divided into two sub-belts, namely, the Eastern and Western Jahazpur belts. The East Jahazpur belt is underlain by Jahazpur granite, indicating major unconformity, and it consists of oligomictic conglomerates, claystone, cherty quartzite, and dolomitic marble (Figure 1). The Western Jahazpur belt is dominated by polymictic conglomerate, dolomites, dolomites with banded iron formation, quartzites, carbonaceous phyllites, conglomerate and grit, and garnetiferous biotite schist [47,61,62].

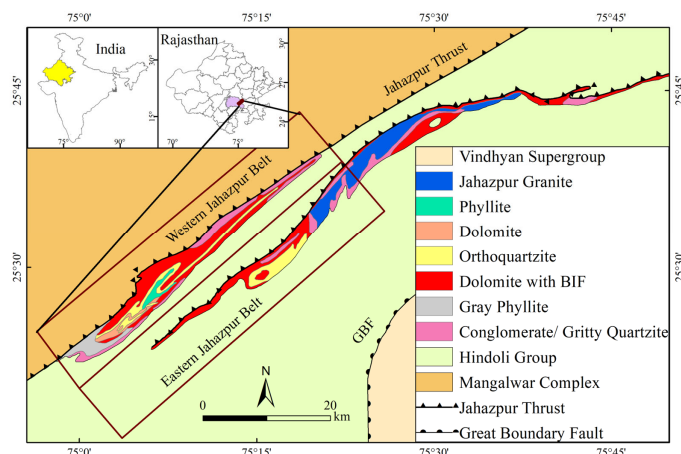


Figure 1. Location and geological map of the study area. The extent of AVIRIS-NG data is overlaid as magenta coloured rectangle. Source: Modified after Gupta et al. [47] and Pandit et al. [61].

Three deformational histories were recorded from the rocks of the Jahazpur Group while the associated basement rocks experienced four deformational events. The regional folding of the Jahazpur rocks was governed by the second generation of the fold, and it produced the interference pattern of Type-2 due to superposed folding with the first generation of the fold at a high angle [59]. The rocks of the Jahazpur region show a NE-SW to ENE-WSW trend. The lineaments are also related to the second generation of folding and are represented by axes of mesofolds, bedding intersections, and schistosity.

Based on rock type variety of phyllosilicates, carbonates and iron oxides are expected. These minerals have diagnostic absorption features in a spectral range of 2.0–2.5 μm , and they can be detected using imaging spectroscopic datasets. Quartz is also expected to present in conglomerates/cherts. However, quartz lacks a diagnostic absorption feature within a spectral range of 0.3–2.5 μm , and thus could not be mapped.

3. Materials and Methodology

3.1. Materials

In this study, we use hyperspectral datasets acquired by AVIRIS-NG in February, 2016 as a part of a joint collaboration between Indian Space Research Organization and National Aeronautics and Space Administration (NASA) in the 0.37–2.5 μm wavelength range, with 425 spectral channels at a spectral resolution of ~ 5 nm and a spatial resolution of 8.1 m [19,37]. The radiance received by sensor has contributions from target material and atmospheric constituents such as aerosols, trace gases, and water vapour. To obtain the surface reflectance of the target materials, the effect of atmospheric constituents is compensated using radiative transfer models. This study used level 2 geocoded surface reflectance product compensated for atmosphere and other artefacts [63,64].

3.2. Mineral Mapping

In the present study, the mineral mapping is carried out by comparing the image and library reflectance spectra containing the characteristic absorption features in the VNIR-SWIR wavelength region, using the least square based complete band shape matching algorithm [18,65]. The central wavelength and FWHM of absorption features are used to draw the candidate minerals from the spectral library. Image (AVIRIS-NG) and USGS library spectra [66] are available at different spectral resolutions and wavelength positions. Therefore, it is important to convolve the library spectra to image spectra prior to the matching of the spectral shapes. The convolution of image and library spectra is performed using Equation (1) [67], assuming a Gaussian response function of AVIRIS-NG sensor.

$$R_i = \frac{\int_{\lambda_1}^{\lambda_2} R_l(\lambda) * S_i(\lambda) d\lambda}{\int_{\lambda_1}^{\lambda_2} S_i(\lambda) d\lambda} \quad (1)$$

where $R_l(\lambda)$ is reflectance at band i and wavelength (λ) , $S_i(\lambda)$ is spectral response function at band i , and $d\lambda$ is the wavelength interval of the sample.

The absorption features of minerals are superimposed over the continuum, which is defined as envelop or global shape of the reflectance spectra. The effect of the continuum needs to be removed prior to spectra matching. The continuum reflectance is estimated in the wavelength range of the diagnostic absorption feature by fitting the straight line between the shoulders of the absorption feature. Subsequently, continuum removed spectra is calculated by dividing the continuum reflectance with observed reflectance values [68]. It should be noted that the continuum is removed only over the spectral range of the diagnostic absorption feature of the image and the library spectra, and not over the entire spectral range of image data.

The depth of the absorption feature is lower (relatively) in the image spectra than in the library, possibly due to the presence of mineral mixtures and surficial weathering. On the contrary, the library spectra are acquired on fresh and powdered samples of pure minerals. To perform the shape matching between the continuum removed image and the library

spectra, the depth of the absorption feature of the image spectra is modified to determine the continuum removed depth (spectral contrast) that maximizes correlation between the image (I) and the library spectra (L). This can be represented by Equations (2)–(6).

$$L = a + bI \quad (2)$$

Here, a and b are constant and are determined using the standard linear least square as:

$$a = (\sum L - b \sum I) / n \quad (3)$$

$$b = \frac{\sum IL - (\sum L \sum I) / n}{\sum L^2 - \frac{(\sum L)^2}{n}} \quad (4)$$

$$b' = \frac{\sum IL - (\sum L \sum I) / n}{\sum I^2 - \frac{(\sum I)^2}{n}} \quad (5)$$

The correlation coefficient (fit value) between the image and library spectra is computed using this equation:

$$F = \sqrt{bb'} \quad (6)$$

The fit value is a metric of the degree of similarity between the image and the library spectra. The fit will be highest if the spectral shape of the image and the library spectra are in close agreement and will have low value otherwise. It should be noted that apart from fit, continuum slope, and wavelength position of the deepest absorption feature, the depth of the absorption feature and the asymmetry of bands are also computed and are used as a constraint to refine the mineral mapping. In the case of minerals having multiple diagnostic absorption features, such as muscovite, whose diagnostic absorption features are located near 2.20 and 2.35 μm , the fit value is computed for both of the absorption features. The final fit (F) is computed as a weighted average of both of the fits (f_1 and f_2). The weights are determined based on relative area of the absorption bands (Equation (7)):

$$F = w_1 f_1 + w_2 f_2 \quad (7)$$

Here, w_1 and w_2 are area normalized weights, are computed from the library spectra, and their sum is one.

The process of the fitting of the image and the library spectra is illustrated by fitting the image spectra of talc with the library spectra of talc, dolomite, and calcite (Figure 2). First, the spectral range of the diagnostic absorption feature of talc is determined based on visual analysis of the spectra. In the case of talc, the diagnostic absorption feature is located within the spectral range of 2.20–2.42 μm . The continuum is removed from the image and the library spectra by fitting a straight line between the shoulders of the absorption feature, with spectral matching then performed, and fit values computed for each fit of the image and the library spectra. The fit value of 0.95, 0.64 and 0.42 are obtained when the image spectra of talc is compared with library spectra of talc (a), dolomite (b), and calcite(c), respectively. Since the fit value is highest for talc, the pixel is identified to contain talc.

In the present study, we use aa USGS library spectra [66] of 30 minerals and compute fit value for each one in the wavelength range of its diagnostic absorption feature at a particular pixel. The library spectra of 30 minerals were selected based on knowledge of the broad lithology of the area, previous hyperspectral based studies, and computational efficiency. The threshold for the fit value is selected as 0.85 [18]. The fit value of more than 0.85 leads to the classification of the pixel; otherwise, it is classified as “unclassified”. This constraint is implemented to enhance the reliability of the mineral map. Apart from this, the constraint on the continuum slope, wavelength position of the diagnostic absorption feature, and depth of the absorption feature are also applied. The slope of the continuum (trend) of the image and the library spectra is compared. If the slope shows large deviations

(more than 30 degrees), no mineral is identified for that fit. Similarly, if the difference in the wavelength position of the deepest absorption feature between the image and the library spectra is more than 10 nm, no mineral identification/classification is conducted. The pixels showing depth of absorption band less than 0.03 are masked out, as they represent low reflectance materials. The spectra of such materials tends to be noisier and may lead to erroneous mineral identification.

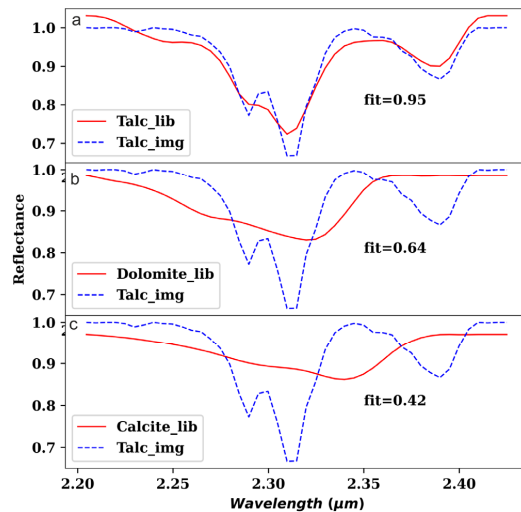


Figure 2. Illustration of complete band shape matching for image spectra of talc with library spectra of talc (a), dolomite (b), and calcite(c) in wavelength range of diagnostic absorption feature.

3.3. Integrated Band Depth

The reflectance spectra of minerals show broad absorption features, which are useful for its identification. Integrated Band Depth (IBD) is an approach to compute the sum of the absorption band depth over a wavelength interval encompassing the selected absorption feature [69]. One of the objectives of the present study was to identify iron-rich zones and study its linkage with talc mineralization. The reflectance spectra of iron-rich minerals such as goethite, hematite, jarosite, and limonite show broad absorption features in the wavelength range of 0.75–1.25 μm , centered near 0.85 μm (Figure 3). To capture this absorption feature, IBD (Equation (8)) is computed by integrating the band depths within the wavelength range of 0.75–1.25 μm .

$$\sum_{d=0}^{d=100} 1 - \frac{R(0.750 + 5n)}{R_c(0.750 + 5n)} \quad (8)$$

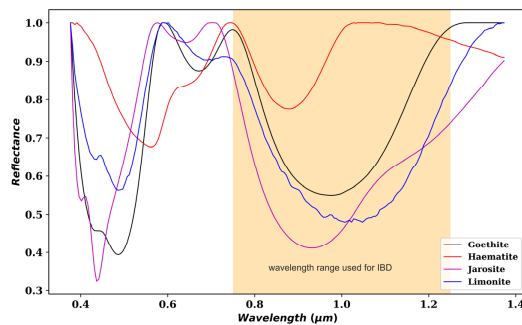


Figure 3. Reflectance spectra of iron-rich minerals goethite, hematite, jarosite, and limonite. The wavelength interval (0.75–1.25 μm) used for calculating the IBD is shaded in orange color.

Here, R refers to reflectance at a given wavelength; R_c is continuum reflectance and is computed as a straight line joining the shoulders of the absorption feature. The spectral

resolution of AVIRIS-NG is 5 nm. Therefore, the absorption bands located every 5 nm are integrated to cover the wavelength up to 1.25 μm. Here, d represents the total number of channels, which is a (or one) hundred in this case. The IBD map thereby generated shows the spatial variation of the depth of absorption feature in the spectral range of 0.75–1.25 μm, and is proportional to iron enrichment. High IBD values indicate significant enrichment of iron oxides, while low values indicate low abundance of iron oxides. It is important to note that IBD in the spectral range of 0.75–1.25 μm is a single value for one pixel, and that it is only to be used to detect the presence of iron enrichment. Unlike mineral mapping, it can not be used for the identification of iron-bearing minerals.

3.4. Masking

The presence of vegetation and water bodies in images obscure the rock surface. In order to avoid erroneous interpretation of mineral and IBD maps, vegetation and water bodies are masked using Normalized Difference Vegetation Index (NDVI) and Normalized Difference Water Index (NDWI), as shown in Equations (9) and (10).

$$NDVI = \frac{NIR - RED}{NIR + RED} \quad (9)$$

$$NDWI = \frac{NIR - SWIR}{NIR + SWIR} \quad (10)$$

For computing $NDVI$, the reflectance value at wavelength 0.66 μm (RED) and 0.84 μm (NIR) were chosen. $NDWI$ is computed using reflectance value at 0.86 (NIR) and 2.10 ($SWIR$) μm. Pixels showing an $NDVI$ value greater than 0.3 and $NDWI$ value greater than 0.20 were masked as they contain vegetation and water bodies and, thus, interpretation was performed on rocky/bare soil pixels only.

4. Results

4.1. Mineral Map

Figure 4 shows the mineral map of the Jahazpur region derived using AVIRIS-NG datasets for minerals showing diagnostic absorption features in the 2.0–2.5 μm spectral range. The data gaps (transparent regions) within the extent of the mineral map represent pixels covered by water and vegetation, and also the pixels where minerals could not be identified reliably. Talc and clay minerals are identified as major minerals present in the region followed by calcite and dolomites. Small exposures of serpentines, particularly on the western side of the Jahazpur thrust, are also noted. The Banas River bed and regions located west of it are dominated by muscovite, while eastern areas of the river bed are dominated by intimate mixtures of kaolinite and muscovite, kaolinite, halloysite, and dickite. All these minerals have spectral signatures that are very similar (common diagnostic absorption at ~2.20 μm) and only differ by the strength of the secondary absorption at 2.16 μm (except for muscovite which has a secondary absorption at ~2.35 μm). The carbonate minerals (dolomite, calcite) and epidote along with chlorite occur in the form of linear patches near the Kachola, Ramgarh, and Beermata locations. The talc mineralization in the region trends NE-SW in accordance with the general strike. Major talc deposits are located in and around Amalda, Ramgarh, and Beermata, and they are hosted by dolomitic rocks. Very few talc mineralizations exist on the eastern part of the Jahazpur thrust. It is important to note that mineral mixtures such as dolomite, calcite, talc, and intimate mixtures of kaolinite and muscovite are identified using the spectra of their mixtures, as provided in the USGS spectral library. The main objective of using the mineral mixture spectra is for confirmation of their presence, and not for quantification of their relative abundance. Furthermore, it is possible that many other minerals may be present in the area, and the present work attempts to identify only the spectrally active minerals. Therefore, the mineral map only indicates the presence of the minerals identified and not their abundance.

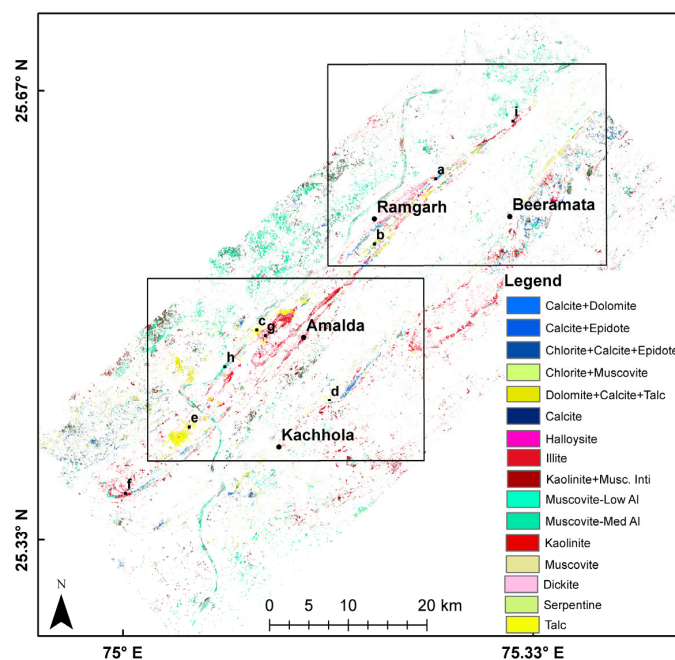


Figure 4. Mineral map of the Jahazpur region. The area is dominated by talc and clay minerals. Two prominent regions of talc mineralization, marked in the rectangle, are investigated for mineralogical and geological control of talc mineralization. Locations (place names) are marked for reference. The image reflectance spectra are collected from locations (a–i) for comparison with library spectra.

4.2. Validation of Mineral Map

In this section, we compare the spectral characteristics of the image and the USGS library spectra of the identified minerals (Figure 5) for locations marked in Figure 4. The image spectra were averaged over 3×3 window for comparison. The reflectance spectra between $2.0\text{--}2.5\ \mu\text{m}$ are, considered for inter-comparison as diagnostic absorption features of identified minerals, are located within this spectral range.

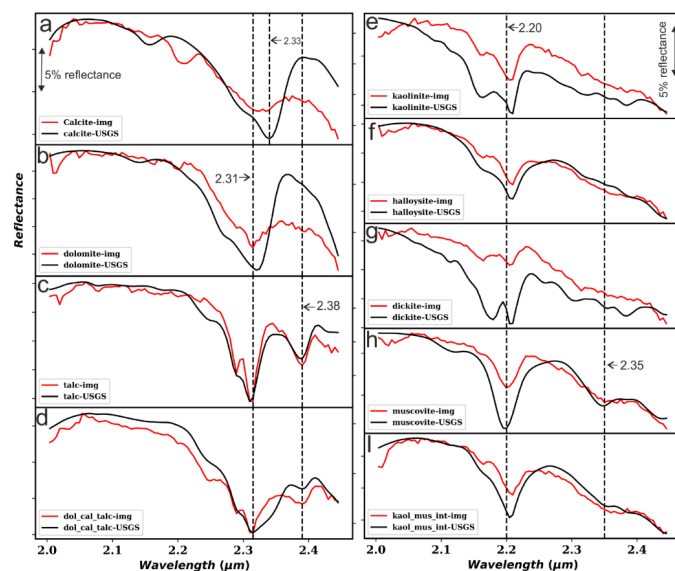


Figure 5. Inter-comparison of reflectance spectra calcite (a), dolomite (b), talc (c), intimate mixture of dolomite, calcite and talc (d), kaolinite (e), halloysite (f), dickite (g), muscovite (h), and intimate mixture of kaolinite and muscovite (i) of image (red) and USGS spectral library (black) for locations marked in Figure 4. The vertical lines are placed at 2.31, 2.33, and 2.38 μm (a–d), and near 2.20 μm for (e–i).

The overall shape of the major absorption feature near 2.33 μm of the image and the library reflectance spectra of calcite (Figure 5a) is in accordance, although a minor absorption feature near 2.12 μm seen in the library spectra is absent in the image spectra. An additional absorption feature located near 2.20 μm in the image spectra may indicate the presence of some clay mineral along with calcite. The image spectra show a relatively higher continuum slope than the library spectra that may indicate differences in weathering [70], which generally mantles the uppermost surface of rocks, differences in geometry of data acquisition or may be related to presence of mineral mixtures.

The image and library reflectance spectra of dolomite are characterized by broad absorption near 2.31 μm due to Mg-OH stretching (Figure 5b). It is important to note that the reflectance spectra of dolomite and calcite show a high degree of similarity in the spectral shape of the absorption feature. However, dolomite can be distinguished from calcite based on a subtle shift in the absorption feature position near 2.31 μm for dolomite versus 2.33 μm for calcite [71].

The reflectance spectra of talc are characterized by a doublet near 2.31 μm and a minor but important diagnostic absorption feature near 2.38 μm [72] (Figure 5c). The shape of major absorption features near 2.31 and 2.38 μm of the image and the library spectra of talc are in close agreement (Figure 5c). The doublet near 2.31 μm is more prominent in the image spectra of talc than the library spectra. This indicates the presence of well-ordered Mg-rich talc compared to the library spectra, where the doublet is feeble [73,74]. The shape of the absorption feature near 2.31 μm is similar for both talc and dolomite. However, talc can be distinguished from spectrally similar dolomite by additional absorption features near 2.25 and 2.38 μm .

The library spectra of dolomite-calcite-talc (mixed in equal proportion) show close similarity with the image spectra (Figure 5d). Both spectra are characterized by major absorption features at 2.31 and 2.38 μm . However, subtle difference in the shape of the absorption feature between the image and the library spectra is observed. This may arise due to the mixing of constituent minerals (dolomite, calcite, and talc) in a different proportion in the image spectra than in the library spectra, or else the presence of minerals that do not have absorption features in the 2.0–2.5 μm spectral range. Nevertheless, based on the similarity of the image and the library spectra, the pixels showing such spectra are classified as an intimate mixture of dolomite-calcite-talc.

The mineral map also showed the presence of various clay minerals such as kaolinite, intimate mixture of kaolinite and muscovite, muscovite, halloysite, and dickite (Figure 4). It is hard to identify the presence of muscovite mixed with kaolinite as they both have an absorption feature at 2.20 μm , akin to montmorillonite/smectites. The main difference is the secondary absorption at 2.35 μm for muscovite or possibly the difference in depth between the 2.16 and 2.2 μm of the kaolinite doublet. The representative reflectance spectra of these minerals are extracted from locations marked in Figure 2 and are compared with the USGS library spectra. It should be noted that the reflectance spectra of clay minerals show absorptions near 1.4 and 1.9 μm related to the presence of OH/H₂O. The contamination of the image spectra by atmospheric residuals at these wavelengths makes the inter-comparison ambiguous. Compensations for atmospheric water vapor absorptions are almost impossible as the amount of water vapor changes through space and time too quickly to be corrected properly. Therefore, the absorption feature near these wavelengths is not considered. The clay minerals lack diagnostic absorption features in 0.4–1.0 μm , and, therefore, this wavelength range is also not considered for inter-comparison.

The image and library spectra of kaolinite show major absorption feature near 2.20 μm and a doublet located at 2.16 μm (Figure 5e). The shape of the absorption feature near 2.20 μm of the image and library spectra are in good agreement, confirming the presence of kaolinite. The reflectance spectrum of halloysite (Figure 5f) is spectrally similar in shape to that of kaolinite. However, the doublet feature near 2.16 μm is more subdued in halloysite than kaolinite, enabling its discrimination from spectrally similar kaolinite. The strength of the doublet near 2.16 μm in kaolinite and halloysite is subtle and depends upon the

crystallinity of kaolinite. Its shows higher strength (more depth) in the reflectance spectra with the well crystallized kaolinite than that of the poorly crystallized kaolinite [75]. Dickite also belongs to the kaolinite group of minerals and shows spectral resemblance to both kaolinite and halloysite (Figure 5g). However, the absorption feature near $2.16\text{ }\mu\text{m}$ is more prominent in dickite and leads to the development of a “w-shaped” feature, which is useful in discriminating it from spectrally similar kaolinite and halloysite. The reflectance spectrum of muscovite is characterised by a symmetrical absorption feature near $2.20\text{ }\mu\text{m}$, and it has a less prominent but still important absorption feature near $2.35\text{ }\mu\text{m}$ (Figure 5h). Since the absorption feature near $2.20\text{ }\mu\text{m}$ is common in other clay minerals, the additional absorption features near $2.35\text{ }\mu\text{m}$ aid in the accurate identification of muscovite. The reflectance spectra of intimately mixed kaolinite and muscovite (Figure 5i) is very similar to that of kaolinite. However, the presence of a noticeable absorption feature near $2.35\text{ }\mu\text{m}$ in an intimate mixture of kaolinite and muscovite distinguishes it from kaolinite.

Overall, the inter-comparison of the library and image reflectance spectra indicates good agreement between the diagnostic absorption features. This indicates the derived mineral map is reliable and can be used for mineral detection and interpretation of alteration patterns.

4.3. Spectroscopic Characterization of Mineralized Area

The reflectance spectra of selected locations from the mineralized zone near Amalda are studied to understand the broad alteration pattern (Figure 6a,b). The reflectance spectra of talc (Talc1 and Talc2) show a clear absorption feature near $0.87\text{ }\mu\text{m}$ in addition to its characteristic doublet near $2.31\text{ }\mu\text{m}$. The reflectance spectra of dolomite, illite, and the intimate mixture of kaolinite and muscovite also show feeble absorption near $0.85\text{ }\mu\text{m}$ in addition to their characteristic absorption feature near 2.33 and $2.20\text{ }\mu\text{m}$. The absorption near $0.85\text{ }\mu\text{m}$ observed in the reflectance spectra of minerals indicates the presence of ferric oxides such as hematite, limonite, and goethite, while the presence of illite and the intimate mixture of kaolinite and muscovite indicates phyllitic and argillitic alteration.

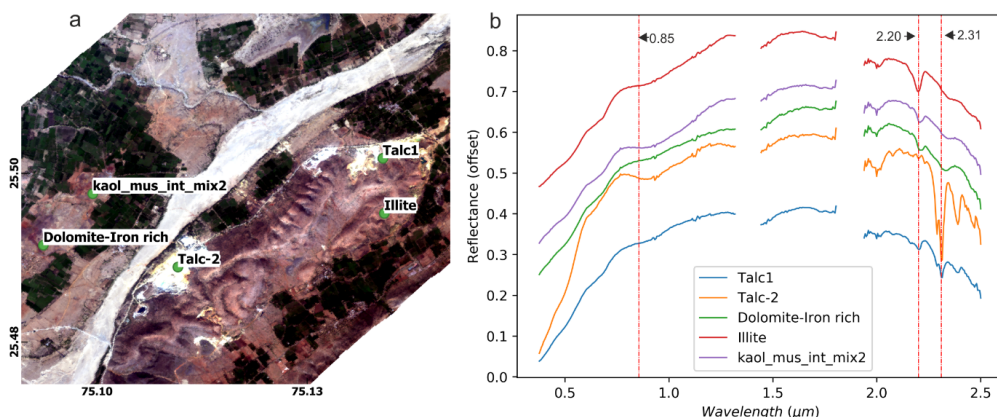


Figure 6. Talc mineralization (seen in bright colour) west of Amalda (a). Reflectance spectra of minerals for locations marked in (a) are shown in (b). The dotted red coloured vertical lines are placed at 0.85 , 2.20 , and $2.31\text{ }\mu\text{m}$.

4.4. Geological and Mineralogical Control of Talc Mineralization

To understand the mineralogical and geological control of talc mineralization, the Amalda and Ramgarh area (Figure 4) are studied as they contain economic mineralization of talc.

4.4.1. Amalda Area

In and around Amalda, the talc mineralization trends NE-SW, following the region's general strike of lithological units. The primary talc mineralization follows the trend of

the Jahazpur thrust, and its occurrence reduces significantly on either side of the thrust. In the eastern parts (west of Amalda), talc dominates spectrally; while near Kachola, spectral signatures of calcites and dolomites along with the talc are noted. The major alteration minerals associated with talc are clay minerals such as the intimate mixture of kaolinite and muscovite, illite, and dickite (Figure 7a) indicating argillic and phyllitic alteration. It should be noted that the talc deposits of the Amalda and Kachola area are located adjacent to quartz-rich lithologies. The IBD map depicting the spatial distribution of iron oxides is shown in Figure 7b. High IBD values indicate iron enrichment and are seen in a reddish tone while zones appearing in greenish tone show the feeble presence of iron oxides. Zones with no data (masked area) of IBD represent vegetated/water-rich areas. It is observed that the major talc deposits in and around Amalda and Kachola show high IBD, indicating the association of iron-rich zones with talc mineralization.

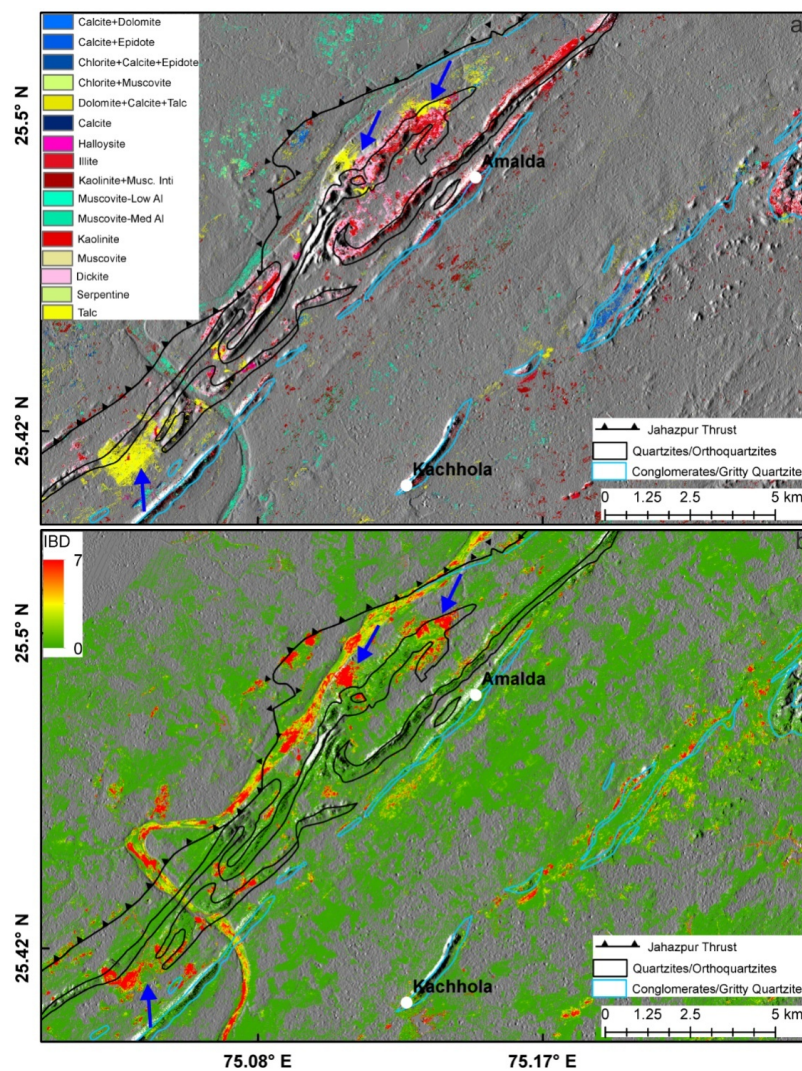


Figure 7. Mineral (a) and IBD for iron oxide (b) map of Amalda area overlaid on Cartosat DEM. The extent of quartz-rich lithologies are overlaid as black (quartzites/orthoquartzites) and blue colored (conglomerates/gritty quartzites) polygons. The Jahazpur thrust (black colored line) is also shown. Blue arrows indicate the regions where talc mineralization is associated with iron enrichment.

4.4.2. Ramgarh Area

Similar to observations of the Amalda region, the talc mineralization in the Ramgarh area is also aligned along the Jahazpur thrust, located in the proximity of conglomerates/gritty quartzites, and is surrounded by clay minerals such as an intimate mixture

of kaolinite and muscovite, illite, and dickite (Figure 8a), indicating phyllitic and argillitic alteration. It is to be noted that the intimate mixtures of calcite, dolomite, and talc are more dominant in Ramgarh as compared to Amalda. This may indicate a more complete conversion of dolomite to talc in Amalda as compared to the Ramgarh area. The IBD map shows significant iron enrichment associated with talc mineralization in the Ramgarh area (Figure 8b).

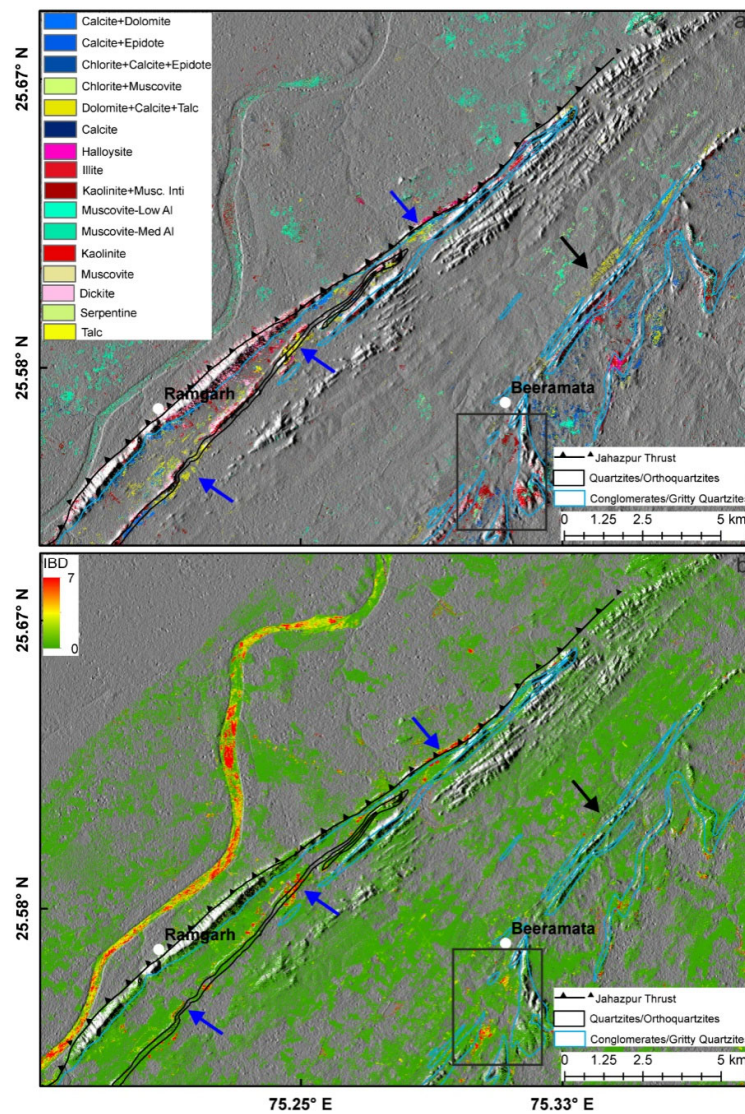


Figure 8. Mineral (a) and IBD for iron oxides (b) map of the Ramgarh area overlaid on Cartosat DEM. The extent of quartz-rich lithologies are overlaid as black (quartzites/orthoquartzites) and blue colored (conglomerates/gritty quartzites) polygons. Jahazpur thrust (black colored line) is also shown. Blue arrows indicate the regions where talc mineralization is associated with iron enrichment. Black arrows indicate regions where talc mineralization is not accompanied by iron enrichment on IBD map.

The talc mineralization in the Beermata region is associated with conglomerates/gritty quartzites, but the IBD map shows no major iron enrichment zones. However, the mineralized area shows the presence of clay minerals such as an intimate mixture of kaolinite and muscovite, illite, and dickite. In contrast, two iron-rich zones located south of Beermata (shown as rectangle in lower left part of Figure 8a,b) show iron enrichment and the presence of clay minerals (as intimate mixture of kaolinite and muscovite, illite, and dickite), and they are also located adjacent to conglomerates/gritty quartzites but do not show a spectral

presence of talc, at least in the upper few microns, which constitutes the vertical depth of investigation in the present study. Since this area shows a phyllitic and argillic alteration pattern, iron enrichment and is located in close proximity to quartz-rich lithologies, it may be considered as prospective zones for future talc exploration projects in the region. It should be noted that the zones of high IBDs along the Banas river bed may not be associated with mineralization, and that they may be indicative of the presence of iron-rich heavy minerals in river/placer deposits.

It is evident from the study that imaging spectroscopy has the potential to characterize the distribution of talc, associated hydrothermal alteration patterns, and iron enrichment. The joint use of the mineral and IBD map can act as an important guide for identifying the possible zone of talc mineralization. In the present study, we note one such zone located south of Beermata, which is located adjacent to silica-rich lithologies, shows iron enrichment, and has a characteristic alteration pattern similar to the known talc mineralization of the Amalda and Ramgarh areas. This may be taken up for a detailed ground-based investigation to prove its potential.

5. Discussion

5.1. Imagining Spectroscopy for Mapping Spectrally Similar Minerals

The high spatial (8 m) spectral resolution (5 nm) of AVIRIS-NG enables better characterization of the shape of absorption features, wavelength position corresponding to absorption minima, and doublets required for reliable and accurate identification of spectrally similar minerals. The focus of the present study is to map the spatial distribution of talc and associated alteration assemblages at high spatial resolution and decipher the process mechanism of talc formation. The talc group of minerals are often associated with serpentine and dolomite because the major mineralization of talc results from the serpentinization process, which involves hydrothermal alteration of ultramafic rocks [76] and the interaction of hydrothermal fluids with dolomites [77]. Though the spectra of talc and host rock (dolomite, serpentine) appear similar, there are subtle differences in the central wavelength of absorption features, the intensity of the doublet, and the spectral shape. In this study, an attempt was made to understand whether AVIRIS-NG with such high spectral resolution can help to discern talc from spectrally similar calcite, dolomite, and serpentines based on the shape of the absorption feature, the wavelength position of absorption minima near 2.31 μm , and the presence of a doublet near 2.27 μm . In addition, this work also explores the relevance of the high spatial resolution of AVIRIS-NG in resolving the alteration minerals, such as kaolinite, muscovite, halloysite, dickite, illite, and an intimate mixture of kaolinite and muscovites, based on subtle differences in the shape of the absorption feature near 2.20 μm and the presence/absence of an absorption feature near 2.35 μm . This is important for deciphering types of hydrothermal alterations (phyllitic, argillic, and advanced argillic), which are characterized by the presence of key minerals such as muscovite, kaolinite, and dickite [78]. The spectral signatures of earth surface materials are complicated due to aerial and intimate mixing [79]. Intimate mixing is inherent to geological materials/rocks, since minerals are mixed at a microscopic scale [80]. The areal mixing arises due to the mixing of two or more materials at a macroscopic scale, such as rock and vegetation, and is less dominant at a finer spatial resolution. Intimate mixing is non-linear, and the abundance of mineral constituents can be obtained through complex unmixing models [81]. In the present study, intimate mixtures of kaolinite and muscovite, calcite and dolomite, and calcite-dolomite-talc are mapped based on matching the image spectra with the library spectra. As mentioned earlier, this study is more about identifying the closely resembling minerals than estimating the mineral abundance.

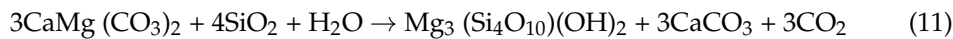
The absorption features of iron oxides such as hematite, goethite, and limonite located near 0.85 μm are broad, and they can be inferred from broadband multispectral remote sensing, too. However, the presence of large (~100 spectral channels) covering broad absorptions near 0.85 μm facilitates better and more reliable quantification of iron oxides. This study also demonstrates the potential of AVIRIS-NG for detailed characterization of

alteration mineral assemblages and gossans in mineralized zones, which is not possible with broadband multispectral instruments. From these perspectives, this study attains significance in understanding the potentials of space-based hyperspectral imagers (e.g., PRISMA, EnMAP), and of airborne (AVIRIS-NG) and drone-based hyperspectral imaging in different scales of mineral mapping and characterization of hydrothermal alteration mineral assemblages, which are important for the discovery of new mineral deposits.

5.2. Mechanism of Talc Formation

The talc mineralization mapped by imaging spectroscopy datasets over the Jahazpur region is hosted by dolomites. The conversion of dolomite to talc is more complete in regions south of Amalda, while in the vicinity of Ramgarh, intimate mixtures of talc, calcite, and dolomite are noted. Major talc deposits are aligned parallel to the Jahazpur thrust, and they are located adjacent to conglomerates/gritty quartzites. Major clay minerals associated with talc mineralization in this region are an intimate mixture of kaolinite and muscovite, illite, and dickite. The iron-rich zones are aligned along the Jahazpur thrust, and they are associated with talc mineralization, especially in and around Amalda.

The majority of the talc mineralization occurs from the hydrothermal alteration of Mg-carbonate and serpentines [82], while some minor deposits can also result from Mg-rich sedimentary rocks [83]. The mineralogy of talc deposits depends on protolith, fluid composition, and pressure/temperature during mineralization. During the metamorphism of siliceous dolomites, talc is one of the first minerals to form [84]. The reaction between dolomite and silica-rich hydrothermal fluid involves the formation of talc and calcite along with release of carbon dioxide (Equation (11)).



Talc mineralization in Jahazpur may have occurred due to the hydrothermal alteration of dolomites. It is plausible that hydrothermal fluid rich in Fe and silica may have reacted with dolomites. The possible fluid sources are granitic intrusion, metamorphic fluid generated by low-grade metamorphism, and fluid circulating in hydrothermal vents of the seafloor. The possibility of granitic intrusion as a fluid source is highly unlikely as the Neoarchean Jahazpur granite is part of the basement and is older than the Jahazpur supracrustal sequence [85]. The other possibility is metamorphic fluid. This may be a plausible source of fluid for talc mineralization as a Jahazpur group of rocks have undergone low-grade greenschist facies of metamorphism [47,61]. The silica, which is one of the prime requirements for talc mineralization within the dolomites, was possibly enriched in metamorphic/hydrothermal fluids by the dissolution of quartz from silica-rich lithologies such as quartzites and conglomerates. The alignment of talc deposits with the Jahazpur thrust suggests that it may have acted as a conduit for hydrothermal fluid.

There is also a strong possibility of talc mineralization by fluid circulating in hydrothermal vents of the seafloor. The dolomites of Jahazpur host low-grade iron deposits and contain iron-rich bands [61,62]. Such iron enrichment of dolomite is often associated with its interaction with iron and silica-rich fluids of hydrothermal vents. The source of iron and silica for the fluid is the leaching of basalts and komatiites, which are part of the ocean floor [86,87]. The presence of Fe^{3+} in tetrahedral and octahedral sites of talc has been reported from talc samples collected from submarine hydrothermal vents [74].

Talc can also form by retrograde reactions from tremolite or high-grade marbles [77,88,89]. However, the presence of tremolite has not been confirmed spectrally, hence the possibility that talc deposit is the result of prograde metamorphism.

6. Conclusions

The talc mineral mapping of Jahazpur shows the presence of talc, dolomite, and calcite along with clay minerals such as kaolinite, muscovite, an intimate mixture of kaolinite and muscovite, illite, dickite, and halloysite. The reflectance spectra of talc show a broad absorption feature near $0.85 \mu\text{m}$ and a doublet near $2.31 \mu\text{m}$, indicating the presence of Fe

in tetrahedral/octahedral sites and well-ordered Mg-rich talc in the region. Analysis of imaging spectroscopic data revealed that two major indicators of talc mineralization are (i) phyllitic and argillitic alteration characterized by the presence of clay minerals, such as an intimate mixture of kaolinite and muscovite, illite, dickite, and halloysite, and (ii) iron enrichment. The enrichment of dolomites by iron possibly indicates hydrothermal fluid circulation. The talc mineralization in the area is also controlled by the Jahazpur thrust and the presence of quartz-rich lithologies. Based on mineralogical evidence derived from imaging spectroscopy and ancillary geological information, the hydrothermal origin of talc mineralization is suggested. This demonstrates the potential of high spatial and spectral resolution imaging spectroscopic data for deciphering the process mechanism of mineralization.

Author Contributions: H.K. designed the study, performed data processing, and wrote the first draft of the manuscript. D.R. contributed to data analysis and interpretation of results. R.J. prepared the geological section and map of the study area. H.G. helped in the interpretation of results. All authors have read and agreed to the published version of the manuscript.

Funding: The authors (H.K. and D.R.) received partial financial support from GAP project (SAC/EPSA/GHCAG/GSD/PP/2019) of Space Applications Centre-ISRO for the research work.

Data Availability Statement: AVIRIS-NG datasets used in this study are available at https://vedas.sac.gov.in/aviris_2.0/sitemap.html.

Acknowledgments: Authors would like to thank Shri Nilesh Desai, I.M. Bahuguna, D.R. Rajak, Former Head/GSD for the support and encouragement provided during the course of study. Efforts of AVIRIS-NG science teams for data acquisition and processing at ISRO and JPL are duly acknowledged.

Conflicts of Interest: The authors declare no conflict of interest.

References

- Ali-Bik, M.W.; Hassan, S.M.; Sadek, M.F. Volcanogenic Talc-Copper Deposits of Darhib-Abu Jurd Area, Egypt: Petrogenesis and Remote Sensing Characterization. *Geol. J.* **2020**, *55*, 5330–5354. [[CrossRef](#)]
- Abrams, M.; Yamaguchi, Y. Twenty Years of ASTER Contributions to Lithologic Mapping and Mineral Exploration. *Remote Sens.* **2019**, *11*, 1394. [[CrossRef](#)]
- Pour, A.B.; Hashim, M. The Application of ASTER Remote Sensing Data to Porphyry Copper and Epithermal Gold Deposits. *Ore Geol. Rev.* **2012**, *44*, 1–9. [[CrossRef](#)]
- Zhang, X.; Pazner, M.; Duke, N. Lithologic and Mineral Information Extraction for Gold Exploration Using ASTER Data in the South Chocolate Mountains (California). *ISPRS J. Photogramm. Remote Sens.* **2007**, *62*, 271–282. [[CrossRef](#)]
- Bedini, E. Mineral Mapping in the Kap Simpson Complex, Central East Greenland, Using HyMap and ASTER Remote Sensing Data. *Adv. Space Res.* **2011**, *47*, 60–73. [[CrossRef](#)]
- Hewson, R.D.; Cudahy, T.J.; Mizuhiko, S.; Ueda, K.; Mauger, A.J. Seamless Geological Map Generation Using ASTER in the Broken Hill-Curnamona Province of Australia. *Remote Sens. Environ.* **2005**, *99*, 159–172. [[CrossRef](#)]
- Rowan, L.C.; Mars, J.C. Lithologic Mapping in the Mountain Pass, California Area Using Advanced Spaceborne Thermal Emission and Reflection Radiometer (ASTER) Data. *Remote Sens. Environ.* **2003**, *84*, 350–366. [[CrossRef](#)]
- Jain, R.; Bhu, H.; Purohit, R. Mapping of the Silica-Rich Rocks and Serpentinites Using Newly Defined Thermal Indices from Advanced Spaceborne Thermal Emission and Reflection Radiometer Thermal Infrared Data of Udaipur-Rakhabdev Region, Rajasthan, India. *J. Appl. Remote Sens.* **2022**, *16*, 034501. [[CrossRef](#)]
- Jain, R. Presence of Base Metals in the Southern Extension of Zawarmala Dolomite, Udaipur, Rajasthan, India. *Curr. Sci.* **2021**, *121*, 962–966. [[CrossRef](#)]
- Jain, R.; Bhu, H.; Purohit, R. ASTER Remote Sensing Data for Delineation of Base Metal—Bearing Dolomites in South-East of Aravalli Craton, India. *Arab. J. Geosci.* **2022**, *15*, 1620. [[CrossRef](#)]
- Guha, A.; Yamaguchi, Y.; Chatterjee, S.; Rani, K.; Vinod Kumar, K. Emittance Spectroscopy and Broadband Thermal Remote Sensing Applied to Phosphorite and Its Utility in Geoexploration: A Study in the Parts of Rajasthan, India. *Remote Sens.* **2019**, *11*, 1003. [[CrossRef](#)]
- Rajendran, S.; Hersi, O.S.; Al-Harthy, A.; Al-Wardi, M.; El-Ghali, M.A.; Al-Abri, A.H. Capability of Advanced Spaceborne Thermal Emission and Reflection Radiometer (ASTER) on Discrimination of Carbonates and Associated Rocks and Mineral Identification of Eastern Mountain Region (Saih Hatat Window) of Sultanate of Oman. *Carbonates Evaporites* **2011**, *26*, 351–364. [[CrossRef](#)]
- Gabr, S.; Ghulam, A.; Kusky, T. Detecting Areas of High-Potential Gold Mineralization Using ASTER Data. *Ore Geol. Rev.* **2010**, *38*, 59–69. [[CrossRef](#)]

14. de Souza Filho, C.R.; Tapia, C.H.; Crósta, A.P.; Xavier, R.P. Infrared Spectroscopy and ASTER Imagery Analysis of Hydrothermal Alteration Zones at the Quellaveco Porphyry-Cooper Deposit, Southern Peru. In Proceedings of the American Society of Photogrammetry and Remote Sensing (ASPRS), Annual Conference—“Technology: Converging at the Top of the World”, Anchorage, AK, USA, 5–9 May 2003; pp. 1–12.
15. Jain, R.; Bhu, H.; Kumar, H.; Purohit, R. Integration of Multi-Sensor Remote Sensing, Geological and Geochemical Data for Delineation of Pb-Zn Bearing Carbonates of Middle Aravalli Group in Zawar–Dungarpur Belt, NW India. *Geocarto Int.* **2022**, *37*, 17165–17199. [[CrossRef](#)]
16. Fereydooni, H.; Mojeddifar, S. A Directed Matched Filtering Algorithm (DMF) for Discriminating Hydrothermal Alteration Zones Using the ASTER Remote Sensing Data. *Int. J. Appl. Earth Obs. Geoinf.* **2017**, *61*, 1–13. [[CrossRef](#)]
17. Ramakrishnan, D.; Bharti, R. Hyperspectral Remote Sensing and Geological Applications. *Curr. Sci.* **2015**, *108*, 879–891.
18. Kumar, H.; Rajawat, A.S. Aqueous Alteration Mapping in Rishabdev Ultramafic Complex Using Imaging Spectroscopy. *Int. J. Appl. Earth Obs. Geoinf.* **2020**, *88*, 102084. [[CrossRef](#)]
19. Jain, R.; Sharma, R.U. Airborne Hyperspectral Data for Mineral Mapping in Southeastern Rajasthan, India. *Int. J. Appl. Earth Obs. Geoinf.* **2019**, *81*, 137–145. [[CrossRef](#)]
20. Jain, R.; Bhu, H.; Purohit, R. Airborne Imaging Spectrometer Dataset for Spectral Characterization and Predictive Mineral Mapping Using Sub-Pixel Based Classifier in Parts of Udaipur, Rajasthan, India. *Adv. Space Res.* **2022**, *in press*. [[CrossRef](#)]
21. Thompson, D.R.; Braverman, A.; Brodrick, P.G.; Candela, A.; Carmon, N.; Clark, R.N.; Connelly, D.; Green, R.O.; Kokaly, R.F.; Li, L.; et al. Quantifying Uncertainty for Remote Spectroscopy of Surface Composition. *Remote Sens. Environ.* **2020**, *247*, 111898. [[CrossRef](#)]
22. Swazye, G.A.; Kokaly, R.F.; Higgins, C.T.; Clinkenbeard, J.P.; Clark, R.N.; Lowers, H.A.; Sutley, S.J. Mapping Potentially Asbestos-Bearing Rocks Using Imaging Spectroscopy. *Geology* **2009**, *37*, 763–766. [[CrossRef](#)]
23. Goetz, A.F.H. Three Decades of Hyperspectral Remote Sensing of the Earth: A Personal View. *Remote Sens. Environ.* **2009**, *113*, S5–S16. [[CrossRef](#)]
24. Hunt, G.W.; Salisbury, J.R. Visible and Near Infrared Spectra of Minerals and Rocks. I. Silicate Minerals. *Mod. Geol.* **1970**, *1*, 283–300.
25. Guha, A.; Ghosh, U.K.; Sinha, J.; Pour, A.B.; Bhaishal, R.; Chatterjee, S.; Baranval, N.K.; Rani, N.; Vinod Kumar, K.; Rao, P.V.N. Potentials of Airborne Hyperspectral AVIRIS-NG Data in the Exploration of Base Metal Deposit—A Study in the Parts of Bhilwara, Rajasthan. *Remote Sens.* **2021**, *13*, 2101. [[CrossRef](#)]
26. Guha, A.; Chatterjee, S.; Oommen, T.; Vinod Kumar, K.; Roy, S.K. Synergistic Use of ASTER, L-Band ALOS PALSAR, and Hyperspectral AVIRIS-NG Data for Exploration of Lode Type Gold Deposit—A Study in Hutt Maski Schist Belt, India. *Ore Geol. Rev.* **2021**, *128*, 103818. [[CrossRef](#)]
27. Wan, Y.-q.; Fan, Y.-h.; Jin, M.-s. Application of Hyperspectral Remote Sensing for Supplementary Investigation of Polymetallic Deposits in Huaniushan Ore Region, Northwestern China. *Nat. Sci. Rep.* **2021**, *11*, 440. [[CrossRef](#)]
28. Pour, A.B.; Zoheir, B.; Pradhan, B.; Hashim, M. Editorial for the Special Issue: Multispectral and Hyperspectral Remote Sensing Data for Mineral Exploration and Environmental Monitoring of Mined Areas. *Remote Sens.* **2021**, *13*, 519. [[CrossRef](#)]
29. Bedini, E.; Chen, J. Application of PRISMA Satellite Hyperspectral Imagery to Mineral Alteration Mapping at Cuprite, Nevada, USA. *J. Hyperspectral Remote Sens.* **2020**, *10*, 87–94. [[CrossRef](#)]
30. van Ruitenbeek, F.J.A.; Cudahy, T.; Hale, M.; van der Meer, F.D. Tracing Fluid Pathways in Fossil Hydrothermal Systems with Near-Infrared Spectroscopy. *Geology* **2005**, *33*, 597. [[CrossRef](#)]
31. Bedini, E. The Use of Hyperspectral Remote Sensing for Mineral Exploration: A Review. *J. Hyperspectral Remote Sens.* **2017**, *7*, 189–211. [[CrossRef](#)]
32. Swazye, G.A.; Smith, K.S.; Clark, R.N.; Sutley, S.J.; Pearson, R.M.; Vance, J.S.; Hageman, P.L.; Briggs, P.H.; Meier, A.L.; Singleton, M.J.; et al. Using Imaging Spectroscopy to Map Acidic Mine Waste. *Environ. Sci. Technol.* **2000**, *34*, 47–54. [[CrossRef](#)]
33. Roache, T.J.; Walshe, J.L.; Huntington, J.F.; Quigley, M.A.; Yang, K.; Bil, B.W.; Blake, K.L.; Hyvärinen, T. Epidote—Clinzoisite as a Hyperspectral Tool in Exploration for Archean Gold. *Aust. J. Earth Sci.* **2011**, *58*, 813–822. [[CrossRef](#)]
34. Keeling, J.; Mauger, A.; Raven, M. Airborne Hyperspectral Survey and Kimberlite Detection in the Terowie District, South Australia. In Proceedings of the CRC LEME Regional Regolith Symposia, Adelaide, SA, Australia, 10–26 November 2004; pp. 166–170.
35. Booyens, R.; Lorenz, S.; Thiele, S.T.; Fuchsloch, W.C.; Marais, T.; Nex, P.A.M.; Gloaguen, R. Accurate Hyperspectral Imaging of Mineralised Outcrops: An Example from Lithium-Bearing Pegmatites at Uis, Namibia. *Remote Sens. Environ.* **2022**, *269*, 112790. [[CrossRef](#)]
36. Khan, S.D.; Jacobson, S. Remote Sensing and Geochemistry for Detecting Hydrocarbon Microseepages. *Geol. Soc. Am. Bull.* **2008**, *120*, 96–105. [[CrossRef](#)]
37. Thompson, D.R.; Thorpe, A.K.; Frankenberg, C.; Green, R.O.; Duren, R.; Guanter, L.; Hollstein, A.; Middleton, E.; Ong, L.; Ungar, S. Space-Based Remote Imaging Spectroscopy of the Aliso Canyon CH₄ Superemitter. *Geophys. Res. Lett.* **2016**, *43*, 6571–6578. [[CrossRef](#)]
38. Roberts, D.A.; Bradley, E.S.; Cheung, R.; Leifer, I.; Dennison, P.E.; Margolis, J.S. Mapping Methane Emissions from a Marine Geological Seep Source Using Imaging Spectrometry. *Remote Sens. Environ.* **2010**, *114*, 592–606. [[CrossRef](#)]

39. Heller Pearlstien, D.; Pignatti, S.; Greisman-Ran, U.; Ben-Dor, E. PRISMA Sensor Evaluation: A Case Study of Mineral Mapping Performance over Makhtesh Ramon, Israel. *Int. J. Remote Sens.* **2021**, *42*, 5882–5914. [[CrossRef](#)]
40. Pignatti, S.; Palombo, A.; Pascucci, S.; Romano, F.; Santini, F.; Simonello, T.; Umberto, A.; Vincenzo, C.; Acito, N.; Diani, M.; et al. The PRISMA Hyperspectral Mission: Science Activities and Opportunities for Agriculture and Land Monitoring. In Proceedings of the 2013 IEEE International Geoscience and Remote Sensing Symposium—IGARSS, Melbourne, VI, Australia, 21–26 July 2013; IEEE: Piscataway, NJ, USA, 2013; pp. 4558–4561.
41. Tripathi, P.; Garg, R.D. First Impressions from the PRISMA Hyperspectral Mission. *Curr. Sci.* **2020**, *119*, 1267–1281. [[CrossRef](#)]
42. Laukamp, C. Geological Mapping Using Mineral Absorption Feature-Guided Band-Ratios Applied to Prisma Satellite Hyperspectral Level 2D Imagery. In Proceedings of the IGARSS 2022—2022 IEEE International Geoscience and Remote Sensing Symposium, Kuala Lumpur, Malaysia, 17 July 2022; IEEE: Piscataway, NJ, USA, 2013; pp. 5981–5984.
43. Nieke, J.; Rast, M. Towards the Copernicus Hyperspectral Imaging Mission for the Environment (CHIME). In Proceedings of the IGARSS 2018—2018 IEEE International Geoscience and Remote Sensing Symposium, Valencia, Spain, 22–27 July 2018; IEEE: Piscataway, NJ, USA; pp. 157–159.
44. Lee, C.M.; Cable, M.L.; Hook, S.J.; Green, R.O.; Ustin, S.L.; Mandl, D.J.; Middleton, E.M. An Introduction to the NASA Hyperspectral InfraRed Imager (HypIRI) Mission and Preparatory Activities. *Remote Sens. Environ.* **2015**, *167*, 6–19. [[CrossRef](#)]
45. GSI. *Geology and Mineral Resources of Rajasthan*, 3rd ed.; Miscellaneous Publication No. 30, Part 12; Geological Survey of India: Jaipur, India, 2011.
46. Jain, R.; Sharma, R.U. Mapping of Mineral Zones Using the Spectral Feature Fitting Method in Jahazpur Belt, Rajasthan, India. *Int. Res. J. Eng. Technol.* **2018**, *5*, 562–567.
47. Gupta, S.N.; Arora, Y.K.; Mathur, R.K.; Iqbaluddin; Prasad, B.; Sahai, T.N.; Sharma, S.B. The Precambrian Geology of the Aravalli Region, Southern Rajasthan & North-Eastern Gujarat. *Mem. Geol. Surv. India* **1997**, *123*, 1–262.
48. Roy, A.B.; Jakhar, S.R. *Geology of Rajasthan (Northwest India): Precambrian to Recent*; Scientific Publishers: Jodhpur, India, 2002; ISBN 81-7233-304-8.
49. Sinha-Roy, S.; Malhotra, G.; Mohanty, M. *Geology of Rajasthan*, 2nd ed.; Geological Society of India: Bangalore, India, 2013.
50. Tripathi, M.K.; Govil, H. Regolith Mapping and Geochemistry of Hydrothermally Altered, Weathered and Clay Minerals, Western Jahajpur Belt, Bhilwara, India. *Geocarto Int.* **2020**, *37*, 879–895. [[CrossRef](#)]
51. Bhadra, B.K.; Pathak, S.; Nanda, D.; Gupta, A.; Srinivasa Rao, S. Spectral Characteristics of Talc and Mineral Abundance Mapping in the Jahazpur Belt of Rajasthan, India Using AVIRIS-NG Data. *Int. J. Remote Sens.* **2020**, *41*, 8754–8774. [[CrossRef](#)]
52. Tripathi, M.K.; Govil, H.; Chatteraj, S.L. Identification of Hydrothermal Altered/Weathered and Clay Minerals through Airborne AVIRIS-NG Hyperspectral Data in Jahajpur, India. *Heliyon* **2020**, *6*, e03487. [[CrossRef](#)]
53. Sunshine, J.M.; Farnham, T.L.; Feaga, L.M.; Groussin, O.; Merlin, F.; Milliken, R.E.; A'Hearn, M.F. Temporal and Spatial Variability of Lunar Hydration as Observed by the Deep Impact Spacecraft. *Science* **2009**, *326*, 565–568. [[CrossRef](#)]
54. Pieters, C.M.; Goswami, J.N.; Clark, R.N.; Annadurai, M.; Boardman, J.; Buratti, B.; Combe, J.-P.; Dyar, M.D.; Green, R.; Head, J.W.; et al. Character and Spatial Distribution of OH/H₂O on the Surface of the Moon Seen by M³ on Chandrayaan-1. *Science* **2009**, *326*, 568–572. [[CrossRef](#)] [[PubMed](#)]
55. Verma, P.K. Deep Continental Structures and Processes in the Aravalli Mountain Range, NW India: Focus on Evolution and Inversion of Regional Faults. *News Lett. DST Gov. India* **1999**, *9*, 197–212.
56. Gupta, S.N.; Arora, Y.K.; Mathur, R.K.; Iqbaluddin; Prasad, B.; Sahai, T.N.; Sharma, S.B. *Lithostratigraphic Map of Aravalli Region, Southern Rajasthan & Northern Gujarat*; Geological Survey: Hyderabad, India, 1980.
57. Mohanty, M.; Guha, D. Lithotectonostratigraphy of the Dismembered Greenstone Sequence of the Mangalwar Complex around Lawa Sardargarh and Parvali Nareas, Rajsamand District, Rajasthan. In *Continental Crust of Northwestern and Central India*; Sinha-Roy, S., Gupta, K.R., Eds.; Memoir of Geological Society of India: Jaipur, India, 1995; Volume 31, pp. 141–162.
58. Reddy, P.R.; Prasad, B.R.; Rao, V.V.; Khare, P.; Rao, G.K.; Murthy, A.S.N.; Sarkar, D.; Raju, S.; Rao, G.S.P.; Sridhar, V. Deep Seismic Reflection Profiling along Nandsi-Kunjer Section of Nagaur-Jhalawar Transect: Preliminary Results. In *Continental Crust of Northwestern and Central India*; Sinha-Roy, S., Gupta, K.R., Eds.; Memoir of Geological Society of India: Jaipur, India, 1995; pp. 353–372.
59. Sinha-Roy, S.; Malhotra, G.; Mohanty, M. *Geology of Rajasthan*; Geological Society of India: Bangalore, India, 1998; ISBN 81-85867-27-5.
60. Roy, A.B.; Purohit, R. *Indian Shield: Precambrian Evolution and Phanerozoic Reconstitution*, 1st ed.; Elsevier Inc.: Cambridge, MA, USA, 2018; ISBN 9780128098394.
61. Pandit, M.K.; Sial, A.N.; Malhotra, G.; Shekhawat, L.S.; Ferreira, V.P. C-, O-Isotope and Whole-Rock Geochemistry of Proterozoic Jahazpur Carbonates, NW Indian Craton. *Gondwana Res.* **2003**, *6*, 513–522. [[CrossRef](#)]
62. Sengupta, S.; Basak, K. Mesoproterozoic Orogeny along the Eastern Boundary of Aravalli Craton, Northwestern India: A Structural and Geochronological Study of Hindoli-Jahazpur Group of Rocks. *J. Earth Syst. Sci.* **2021**, *130*, 203. [[CrossRef](#)]
63. Thompson, D.R.; Gao, B.C.; Green, R.O.; Roberts, D.A.; Dennison, P.E.; Lundein, S.R. Atmospheric Correction for Global Mapping Spectroscopy: ATREM Advances for the HypIRI Preparatory Campaign. *Remote Sens. Environ.* **2015**, *167*, 64–77. [[CrossRef](#)]
64. Mishra, M.K.; Gupta, A.; John, J.; Shukla, B.P.; Dennison, P.; Srivastava, S.S.; Kaushik, N.K.; Misra, A.; Dhar, D. Retrieval of Atmospheric Parameters and Data-Processing Algorithms for AVIRIS-NG Indian Campaign Data. *Curr. Sci.* **2019**, *116*, 1089–1100. [[CrossRef](#)]

65. Clark, R.N.; Swayze, G.A.; Livo, K.E.; Kokaly, R.F.; Sutley, S.J.; Dalton, J.B.; McDougal, R.R.; Gent, C.A. Imaging Spectroscopy: Earth and Planetary Remote Sensing with the USGS Tetracorder and Expert Systems. *J. Geophys. Res.* **2003**, *108*, 5131. [[CrossRef](#)]
66. Kokaly, R.F.; Clark, R.N.; Swayze, G.A.; Livo, K.E.; Hoefen, T.M.; Pearson, N.C.; Wise, R.A.; Benzel, W.M.; Lowers, H.A.; Driscoll, R.L.; et al. *USGS Spectral Library*, Version 7. U.S. Geological Survey Data Series 1035, U.S. Geological Survey: Reston, VA, USA, 2017. [[CrossRef](#)]
67. Richter, R. Correction of Atmospheric and Topographic Effects for High Spatial Resolution Satellite Imagery. *Int. J. Remote Sens.* **1997**, *18*, 1099–1111. [[CrossRef](#)]
68. Clark, R.N.; Roush, T.L. Reflectance Spectroscopy: Quantitative Analysis Techniques for Remote Sensing Applications. *J. Geophys. Res. Solid Earth* **1984**, *89*, 6329–6340. [[CrossRef](#)]
69. Mustard, J.F.; Pieters, C.M.; Isaacson, P.J.; Head, J.W.; Besse, S.; Clark, R.N.; Klima, R.L.; Petro, N.E.; Staid, M.I.; Sunshine, J.M.; et al. Compositional Diversity and Geologic Insights of the Aristarchus Crater from Moon Mineralogy Mapper Data. *J. Geophys. Res.* **2011**, *116*, E00G12. [[CrossRef](#)]
70. Nettles, J.W.; Staid, M.; Besse, S.; Boardman, J.; Clark, R.N.; Dhingra, D.; Isaacson, P.; Klima, R.; Kramer, G.; Pieters, C.M.; et al. Optical Maturity Variation in Lunar Spectra as Measured by Moon Mineralogy Mapper Data. *J. Geophys. Res.* **2011**, *116*, E00G17. [[CrossRef](#)]
71. Gaffey, S.J. Spectral Reflectance of Carbonate Minerals in the Visible and near Infrared (0.35–2.55 Microns); Calcite, Aragonite, and Dolomite. *Am. Mineral.* **1986**, *71*, 151–162.
72. Petit, S.; Martin, F.; Wiewiora, A.; De Parseval, P.; Decarreau, A. Crystal-Chemistry of Talc: A Near Infrared (NIR) Spectroscopy Study. *Am. Mineral.* **2004**, *89*, 319–326. [[CrossRef](#)]
73. Michalski, J.R.; Cuadros, J.; Bishop, J.L.; Darby Dyar, M.; Dekov, V.; Fiore, S. Constraints on the Crystal-Chemistry of Fe/Mg-Rich Smectitic Clays on Mars and Links to Global Alteration Trends. *Earth Planet. Sci. Lett.* **2015**, *427*, 215–225. [[CrossRef](#)]
74. Cuadros, J.; Dekov, V.M.; Fiore, S. Crystal Chemistry of the Mixed-Layer Sequence Talc-Talc-Smectite-Smectite from Submarine Hydrothermal Vents. *Am. Mineral.* **2008**, *93*, 1338–1348. [[CrossRef](#)]
75. Pineau, M.; Mathian, M.; Baron, F.; Rondeau, B.; Le Deit, L.; Allard, T.; Mangold, N. Estimating Kaolinite Crystallinity Using Near-Infrared Spectroscopy: Implications for Its Geology on Earth and Mars. *Am. Mineral.* **2022**, *107*, 1453–1469. [[CrossRef](#)]
76. Holm, N.G.; Oze, C.; Mousis, O.; Waite, J.H.; Guillet-Lepoutre, A. Serpentinization and the Formation of H₂ and CH₄ on Celestial Bodies (Planets, Moons, Comets). *Astrobiology* **2015**, *15*, 587–600. [[CrossRef](#)] [[PubMed](#)]
77. Hecht, L.; Freiberger, R.; Gilg, H.A.; Grundmann, G.; Kostitsyn, Y.A. Rare Earth Element and Isotope (C, O, Sr) Characteristics of Hydrothermal Carbonates: Genetic Implications for Dolomite-Hosted Talc Mineralization at Gopfersgrun (Fichtelgebirge, Germany). *Chem. Geol.* **1999**, *155*, 115–130. [[CrossRef](#)]
78. Swayze, G.A.; Clark, R.N.; Goetz, A.F.H.; Livo, K.E.; Breit, G.N.; Kruse, F.A.; Sutley, S.J.; Snee, L.W.; Lowers, H.A.; Post, J.L.; et al. Mapping Advanced Argillic Alteration at Cuprite, Nevada, Using Imaging Spectroscopy. *Econ. Geol.* **2014**, *109*, 1179–1221. [[CrossRef](#)]
79. Heylen, R.; Gader, P. Nonlinear Spectral Unmixing With a Linear Mixture of Intimate Mixtures Model. *IEEE Geosci. Remote Sens. Lett.* **2014**, *11*, 1195–1199. [[CrossRef](#)]
80. Ducasse, E.; Adeline, K.; Briottet, X.; Hohmann, A.; Bourguignon, A.; Grandjean, G. Montmorillonite Estimation in Clay-Quartz-Calcite Samples from Laboratory SWIR Imaging Spectroscopy: A Comparative Study of Spectral Preprocessings and Unmixing Methods. *Remote Sens.* **2020**, *12*, 1723. [[CrossRef](#)]
81. Wang, D.; Shi, Z.; Cui, X. Robust Sparse Unmixing for Hyperspectral Imagery. *IEEE Trans. Geosci. Remote Sens.* **2018**, *56*, 1348–1359. [[CrossRef](#)]
82. El-Sharkawy, M.F. Talc Mineralization of Ultramafic Affinity in the Eastern Desert of Egypt. *Miner. Depos.* **2000**, *35*, 346–363. [[CrossRef](#)]
83. Joshi, P.; Pant, P.D.; Upadhyaya, R.C. Petrography and Geochemistry of Magnesite and Talc Deposits of Jhironi, Kumaun Lesser Himalaya. In *Migmatism, Tectonism And Mineralization*; Kumar, S., Ed.; Macmillan Publishers India Ltd.: New Delhi, India, 2009.
84. Winter, J.D. *An Introduction to Igneous and Metamorphic Petrology*, 1st ed.; Pearson College Div: Prentice Hall Upper Saddle River, NJ, USA, 2001.
85. Dey, B.; Das, K.; Dasgupta, N.; Bose, S.; Hidaka, H.; Ghatak, H. Zircon U-Pb (SHRIMP) Ages of the Jahazpur Granite and Mangalwar Gneiss from the Deoli-Jahazpur Sector, Rajasthan, NW India: A Preliminary Reappraisal of Stratigraphic Correlation and Implications to Crustal Growth. In *Geological Evolution of the Precambrian Indian Shield*. Society of Earth Scientists Series; Mondal, M.E.A., Ed.; Springer: Cham, Switzerland, 2019; pp. 39–56.
86. Klein, C.; Ladeira, E.A. Geochemistry and Petrology of Some Proterozoic Banded Iron-Formations of the Quadrilatero Ferrifero, Minas Gerais, Brazil. *Econ. Geol.* **2000**, *95*, 405–427. [[CrossRef](#)]
87. Bau, M.; Möller, P. Rare Earth Element Systematics of the Chemically Precipitated Component in Early Precambrian Iron Formations and the Evolution of the Terrestrial Atmosphere-Hydrosphere-Lithosphere System. *Geochim. Cosmochim. Acta* **1993**, *57*, 2239–2249. [[CrossRef](#)]

88. Shin, D.; Lee, I. The Fluid Evolution Related to Talc Mineralization in the Hwanggangri Area, South Korea. *Resour. Geol.* **2002**, *52*, 273–278. [[CrossRef](#)]
89. Anderson, D.L.; Mogk, D.W.; Childs, J.F. Petrogenesis and Timing of Talc Formation in the Ruby Range, Southwestern Montana. *Econ. Geol.* **1990**, *85*, 585–600. [[CrossRef](#)]

Disclaimer/Publisher's Note: The statements, opinions and data contained in all publications are solely those of the individual author(s) and contributor(s) and not of MDPI and/or the editor(s). MDPI and/or the editor(s) disclaim responsibility for any injury to people or property resulting from any ideas, methods, instructions or products referred to in the content.